

# CO<sub>2</sub> hydrogenation to methanol using Cu-Zn catalyst supported on reduced graphene oxide nanosheets



Varisara Deerattrakul<sup>a</sup>, Peerapan Dittanet<sup>b</sup>, Montree Sawangphruk<sup>c</sup>,  
Paisan Kongkachuichay<sup>a,\*</sup>

<sup>a</sup> Department of Chemical Engineering, Faculty of Engineering, NANOTEC Center for Nanoscale Materials Design for Green Nanotechnology and Center for Advanced Studies in Nanotechnology and its Applications in Chemical, Food and Agricultural Industries, Kasetsart University, Bangkok 10900, Thailand

<sup>b</sup> Department of Chemical Engineering, Faculty of Engineering and Center for Advanced Studies in Industrial Technology, Kasetsart University, Bangkok 10900, Thailand

<sup>c</sup> School of Energy Science and Engineering, Vidyasirimedhi Institute of Science and Technology, Wangchan, Rayong 21210, Thailand

## ARTICLE INFO

### Article history:

Received 1 April 2016

Received in revised form 30 June 2016

Accepted 6 July 2016

Available online 15 July 2016

### Keywords:

Hydrogenation

Methanol

Carbon dioxide

Cu

Zn

Graphene oxide

## ABSTRACT

Supported Cu-Zn/reduced graphene oxide (rGO) catalysts were synthesized via an incipient wetness impregnation and evaluated for a CO<sub>2</sub> hydrogenation to methanol. The structure, surface reactivity, and adsorption properties were investigated extensively by FE-SEM, TEM, XRD, Raman, FT-IR, N<sub>2</sub> sorption, TGA, TPR, and XPS techniques. The effects of Cu-Zn metal loading content and the reaction temperature were investigated toward the methanol production from the CO<sub>2</sub> hydrogenation. It was found that supported rGO nanosheets could greatly enhance the catalytic performance and help the dispersion of bimetallic compounds Cu-Zn particles. The 10 wt%CuZn/rGO catalyst yielded the highest space time yield (STY) of 424 mg<sub>MeOH</sub> g<sub>cat</sub><sup>-1</sup> h<sup>-1</sup> at a reaction temperature and pressure of 250 °C and 15 bar, respectively.

© 2016 Elsevier Ltd. All rights reserved.

## 1. Introduction

Recently, global warming has become a serious problem affecting humanity due to a rapid increase of CO<sub>2</sub> emission which has consequently led to an increase in the average global temperature [1]. Therefore, various techniques have been proposed to reduce the atmospheric CO<sub>2</sub> accumulation, for example: carbon capture and storage (CCS) [2–4] that aims to capture and store large quantities of CO<sub>2</sub>, and carbon capture and utilization (CCU) [5–7] that aims to convert CO<sub>2</sub> to fuels such as dimethyl ether (DME) dimethyl carbonate (DMC), and methanol (MeOH) [8–13]. Especially for the production in the latter case, DME, DMC, and MeOH are key feedstock for industrial chemicals, which can be converted into high molecular weight hydrocarbons and alternative fuels, where the CO<sub>2</sub> hydrogenation process is one of the most efficient and economical routes for CO<sub>2</sub> emission utilization [14–20]. However, the hydrogenation reaction is highly exothermic and it is difficult to activate CO<sub>2</sub> owing to its high stability [21,22]. Therefore, catalysts are employed to reduce the activation energy of the hydrogenation step and break the CO<sub>2</sub> bonds [23,24].

Cu-Zn oxide-based catalysts have been widely reported for the CO<sub>2</sub> hydrogenation to methanol process [25–30]. The role of Zn oxide is to improve the dispersion of metallic copper particles. Additionally, it has been found that Zn oxide exhibits an active site for hydrogen spillover. Moreover, the interaction between Cu and Zn oxide causes an electron transfer from Zn oxide to Cu metal that occurs as Cu<sup>0</sup> and Cu<sup>+</sup> species, which are crucial for CO<sub>2</sub> hydrogenation to methanol [31–36]. It has been confirmed by other studies that copper metal alone cannot be the sole active site for higher activities in methanol synthesis [37,38]. While Cu-Zn oxide-based catalysts have been well-researched for methanol synthesis, these catalysts are not prevalent because the metals have low active surface area and are prone to sintering.

Hence, catalyst supports are used as a metal receptor to increase surface area and improve metal dispersion [39–43]. Carbon materials such as carbon nanotubes (CNTs) and activated carbon (AC) have been commonly used as the catalyst supports due to their attractive physical and thermal properties such as high surface area (i.e., 180–200 m<sup>2</sup> g<sup>-1</sup> [44–47]), uniform and straight pores, inert graphitic surface, and high thermal stability, while also exhibiting good performance for adsorption of hydrogen [48–51]. However, CNTs and AC still have lower specific surface areas when compared with graphene [50].

\* Corresponding author.

E-mail address: [paisan.k@ku.ac.th](mailto:paisan.k@ku.ac.th) (P. Kongkachuichay).

The unique physical, chemical, and mechanical properties of graphene make it an ideal support material for the catalysts such as high theoretical surface area of  $2630\text{ m}^2\text{ g}^{-1}$ , which provides an attractive platform for surface interactions and surface chemistry, tensile strength of 130 GPa, thermal conductivity of  $4840\text{--}5300\text{ W m K}^{-1}$ , and electron mobility of  $15,000\text{ cm}^2\text{ V}^{-1}$  [52–57]. Beside, graphene has been used worldwide as a catalytic support material for various chemical reactions and used in photoelectric catalysis, lithium ion battery, and fuel cell.

In this work, supported Cu–Zn on reduced graphene oxide (rGO) catalysts were synthesized via incipient wetness impregnation and evaluated for CO<sub>2</sub> hydrogenation to methanol. The supporting materials were synthesized via an oxidation of graphite to graphene oxide, followed by a chemical reduction method. The reaction temperature and percent loading of the bimetallic Cu–Zn compounds on the graphene support were finely tuned to achieve the high performance of CO<sub>2</sub> hydrogenation to methanol.

## 2. Experimental

### 2.1. Chemicals and materials

The chemicals used in this study were graphite powder (20–40  $\mu\text{m}$ , Sigma Aldrich), sodium nitrate (99.5% NaNO<sub>3</sub>, Qrec),

potassium permanganate (99% KMnO<sub>4</sub>, Ajax Finechem), sulfuric acid (98% H<sub>2</sub>SO<sub>4</sub>, Qrec), hydrogen peroxide (30% H<sub>2</sub>O<sub>2</sub>, Merck), hydrazine hydrate (80% N<sub>2</sub>H<sub>4</sub>, Merck), copper nitrate trihydrate (99.5% Cu(NO<sub>3</sub>)<sub>2</sub>·3H<sub>2</sub>O, Qrec), zinc nitrate hexahydrate (98% Zn(NO<sub>3</sub>)<sub>2</sub>·6H<sub>2</sub>O, Lobachemie), and water, which was purified via a Milli-Q system ( $>18\text{ M}\Omega\text{ cm}$ , Millipore).

### 2.2. Preparation of rGO

Graphene oxide (GO) was synthesized according to the modified Hummers method [58], with additional modifications following Sawangphruk et al. [59]. First, graphite powder (5.0 g) and NaNO<sub>3</sub> (7.5 g) were mixed in H<sub>2</sub>SO<sub>4</sub> (500 ml). Then, KMnO<sub>4</sub> (40.0 g) was slowly added under stirring at 200 rpm in an ice bath for 24 h. Water (500 ml) and H<sub>2</sub>O<sub>2</sub> (150 ml) were added into mixture solution in an ice bath under stirring at 200 rpm for 24 h. The product was collected by centrifuge and washed with water several times until the pH was neutral. The as-synthesized product was dried at 50 °C for 24 h. Next, rGO was prepared via a chemical reduction of GO. First, the as-prepared GO (1.0 g) was dispersed in 300 ml of water under sonication for 1 h. Then, hydrazine (30 ml) was added into the suspension while stirring at 200 rpm at 98 °C for 24 h to eliminate oxygen functional groups. Finally, the as-synthesized product was collected via vacuum filtration and

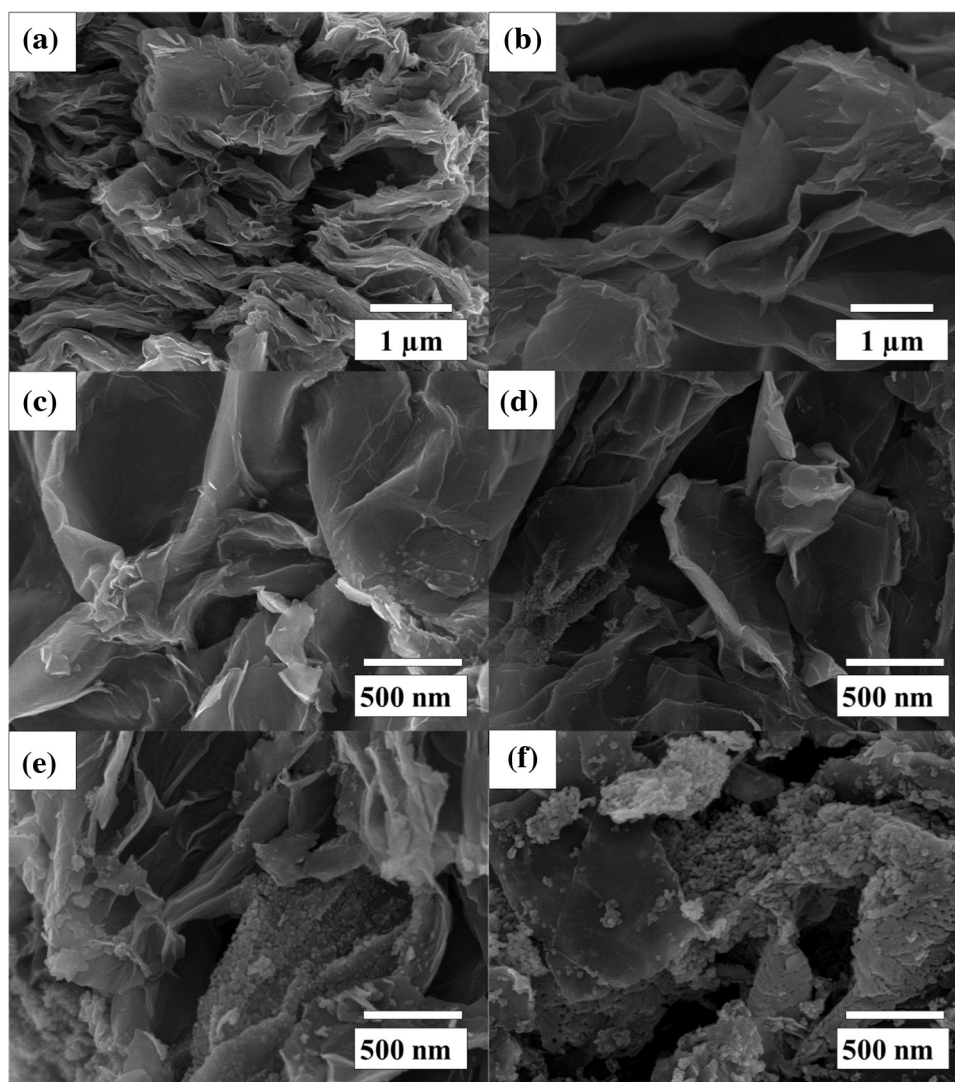


**Fig. 1.** SEM images of (a) rGO, (b) calcined rGO, (c) 5%CuZn/rGO, (d) 10%CuZn/rGO, (e) 20%CuZn/rGO, and (f) 30%CuZn/rGO.

washed with water to remove the residual reducing agent. The as-synthesized rGO was dried at 50 °C for 24 h.

### 2.3. Preparation of Cu-Zn/rGO

The catalysts were prepared with different weight percentages of 5, 10, 20, and 30 Cu-Zn metals, with equimolar of Cu-Zn with rGO support via an incipient wetness impregnation. Subsequently, the as-prepared catalysts were dried at 100 °C for 12 h and calcined in air at 350 °C for 2 h with a heating rate of 2 °C min<sup>-1</sup> to eliminate impurities and form surface metal oxides.

### 2.4. Catalyst characterization

The surface morphology of obtained catalysts was observed with a field emission scanning electron microscope (FE-SEM) and a transmission electron microscopy (TEM). X-ray diffraction (XRD) patterns were characterized by using an X-ray diffractometer (XRD, Philips X-Pert) with Cu K $\alpha$  radiation source ( $\lambda_{K\alpha} = 1.54 \text{ \AA}$ ) at an angle in the  $2\theta$  range of 5–90°, 40 kV, 30 mA, with a scan rate of 2° min<sup>-1</sup>. Raman spectra of graphene-based materials were analyzed with a Senterra Dispersive Raman Microscope (Bruker

Optics) with laser (532 nm). Fourier-transform infrared (FT-IR) spectra were measured with a spectrophotometer (Bruker Tensor 27) in the range of 400–4000 cm<sup>-1</sup>, with a resolution of 4 cm<sup>-1</sup> to investigate the chemical bonds formed. The specimens were prepared by grinding the samples together with potassium bromide (KBr) and compressing them into thin pellets. The BET surface area ( $S_{\text{BET}}$ ), nitrogen adsorption isotherms, pore size distribution, and pore volume ( $V_p$ ) of as-synthesized catalysts were measured with the N<sub>2</sub>-sorption measurement (Quantachrome Autosorp-1C instrument) at –196 °C.

The thermogravimetric analyzer (TGA, Perkin Elmer STD 2960) measured the thermal decomposition of the as-synthesized catalysts. The samples were loaded into an alumina pan and heated in a flow of ambient air from 25 to 600 °C with a heating rate of 10 °C min<sup>-1</sup>. The reduction temperature of as-synthesized catalysts was obtained by temperature-programmed reduction (TPR). Measurements were performed at 25–800 °C in a continuous flow apparatus using an Inconel-tube reactor (Inconel-600, O. D. 3/8 in.). For this experiment, the mixture of H<sub>2</sub> and Ar (9.6% H<sub>2</sub> balanced with Ar) was fed into the catalyst bed. H<sub>2</sub> consumption was monitored by using a Shimadzu gas chromatograph (GC-2014) equipped with a thermal conductivity detector (TCD). The surface

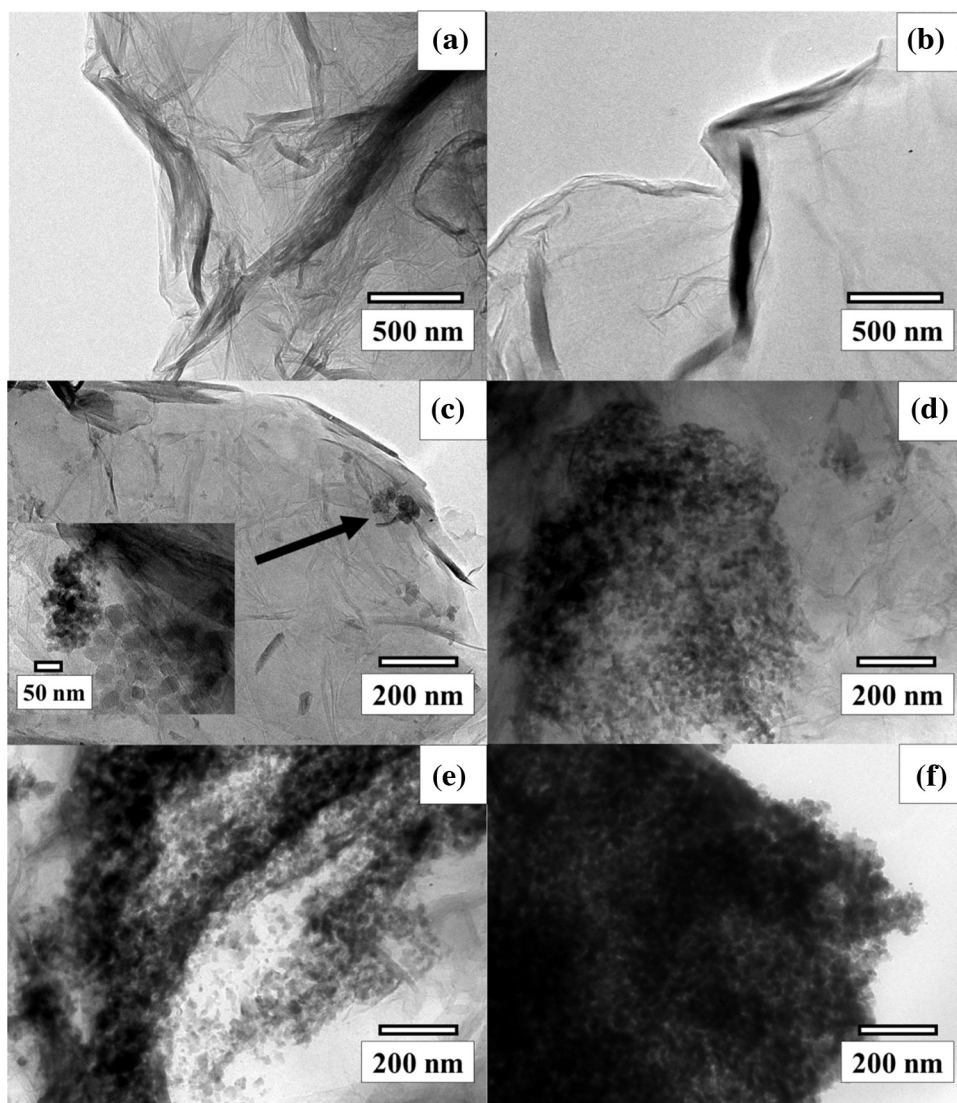


Fig. 2. TEM images of (a) rGO, (b) calcined rGO, (c) 5%CuZn/rGO, (d) 10%CuZn/rGO, (e) 20%CuZn/rGO and (f) 30%CuZn/rGO.

analysis was performed using X-ray photoelectron spectroscopy (XPS) for investigating the oxidation state of Cu-Zn, chemical bonding and chemical composition that compromise between the theoretical and actual metal loading composition.

### 2.5. Catalytic activity test

The catalytic testing in the CO<sub>2</sub> hydrogenation reaction was performed in a tubular stainless steel fixed-bed reactor. 0.25 g of the catalyst was in-situ reduced at 350 °C for 2 h with flowing H<sub>2</sub> (40 ml min<sup>-1</sup>). Then, the temperature was cooled to the desired reaction temperature. After that, a gas mixture CO<sub>2</sub>/H<sub>2</sub> = 1/3 (GHSV = 2400 h<sup>-1</sup>) was fed to the reactor. The reaction pressure was raised to 15 bar and the gaseous products were analyzed with a gas chromatograph (Shimadzu, GC-14A equipped in a Unibead-C packed column with TCD and a Porapak Q column with FID).

## 3. Results and discussion

### 3.1. Catalyst characterization results

Fig. 1 shows the apparent morphologies of the catalyst samples evaluated with FE-SEM measurements. The images reveal a large number of rGO nanosheets as anchoring sites from the catalyst support. Meanwhile, 5, 10, 20, and 30% of Cu-Zn/rGO catalyst samples exhibit Cu-Zn metals on rGO nanosheets. FE-SEM images of Fig. 1c–f clearly show that increasing the percent loading of bimetallic compounds of Cu-Zn leads to more aggregation of the active metals.

TEM images of the catalyst samples are shown in Fig. 2. From the TEM images of rGO and rGO after calcination (Fig. 2a and b, respectively), both rGO and calcined rGO have a wrinkled morphology caused by a few layers of rGO nanosheets having restacked. After calcination, the wrinkled morphology decreases, revealing the advantage for rGO structure. In the TEM images of 5, 10, 20, and 30% of CuZn/rGO catalyst samples, Cu-Zn particles were found to be coated on the surfaces of rGO. With increasing percent loading of bimetallic compounds of Cu-Zn, the particles appeared to form increasingly small aggregates, as shown in Fig. 2c–f.

The reduction of GO into rGO was also investigated with the X-ray diffraction (XRD) technique. The XRD patterns of the catalyst samples are shown in Fig. 3. The peak pattern of GO, which is similar to the standard reference peak [60], is shown in Fig. 3a. Under reduction conditions, the main peak for GO at ~10° is shifted to ~26°, which is assigned to the graphitic planes (002) of the graphene nanosheets, indicating that GO was reduced to graphene [61]. Following the loading of bimetallic compounds Cu-Zn, the

new peaks from the diffraction pattern correspond to the crystal phases of CuO and ZnO, which are clearly visible. The calcination and loading of bimetallic compounds Cu-Zn do not alter the structure of rGO as the peak patterns of rGO still remain, but the intensity is slightly reduced due to metal coverage, as expected (Fig. 3c–g). These results are also confirmed by the Raman spectrometer. Moreover, the size of the graphitic crystallites ( $L_a$ ) and the stacking height ( $L_c$ ) in the rGO support can be calculated from the (002) graphitic peak and the (100) planes, respectively using the Scherrer equation, and the  $d$ -spacing in the rGO support can be approximated by the Bragg's Law as described by the following equations [62–64]:

$$L_a = \frac{1.84\lambda_{K\alpha}}{\beta \cos \theta} \quad (1)$$

$$L_c = \frac{0.89\lambda_{K\alpha}}{\beta \cos \theta} \quad (2)$$

$$2d \sin \theta = n\lambda \quad (3)$$

where  $\beta$  is the full width at half-maximum (FWHM) of the (002) and (100) peaks. The graphitic crystallite size was determined to be 4.5 nm for rGO, 5.4 nm for rGO after calcination, and 4.9 nm for rGO after loading of Cu-Zn. The stacking height of rGO and rGO after calcination are 3.4 and 3.6 nm, respectively. Meanwhile, the stacking heights of 5, 10, 20, and 30% of Cu-Zn/rGO catalyst samples are 4.5, 5.3, 5.8, and 6.0 nm, respectively. This increase of height was attributed to the insertion of Cu-Zn particles between the rGO nanosheets. Additionally, the  $d$ -spacing of the rGO support was found to be about 2 Å.

Raman spectroscopy was utilized to identify the structure and degree of disorder in carbon-based materials of the graphitic support, both before and after metal impregnation. The Raman spectra of the catalyst samples are shown in Fig. 4. Typically, GO and rGO show a strong disorder in the lattice of the sp<sup>3</sup>-hybridized carbon atoms, a so-called D band, and an in-plane bond-stretching motion of pairs of sp<sup>2</sup> carbon atoms, namely G band [65], that occur at about 1350 cm<sup>-1</sup> and 1585 cm<sup>-1</sup>, respectively [66]. After calcination and loading of bimetallic compounds Cu-Zn, the Raman spectra reveal similar D and G bands at about 1350 and 1585 cm<sup>-1</sup>, respectively. The D/G intensity ratio of all catalysts is approximately 1, which is consistent with the previous study [67]. The intensity of the D band is slightly higher than the G band; therefore, it can be deduced that rGO has many smaller graphitic sheets [68]. Furthermore, the crystallite size ( $L_a$ ) can be calculated

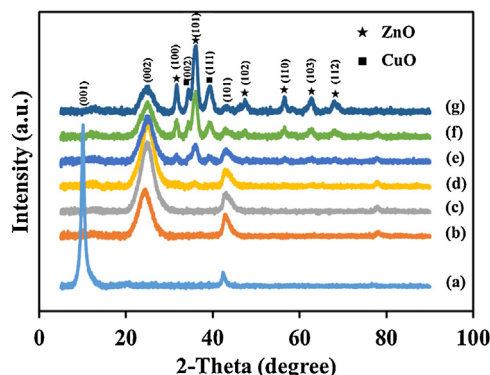


Fig. 3. XRD patterns of (a) GO, (b) rGO, (c) calcined rGO, (d) 5%CuZn/rGO, (e) 10% CuZn/rGO, (f) 20%CuZn/rGO and (g) 30%CuZn/rGO.

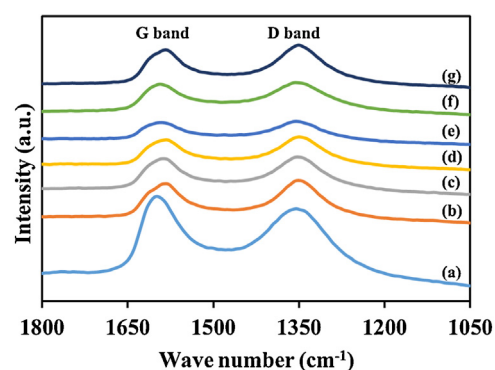
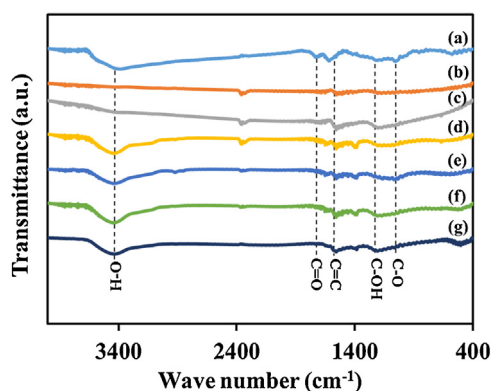


Fig. 4. Raman spectra of (a) GO, (b) rGO, (c) calcined rGO, (d) 5% CuZn/rGO, (e) 10% CuZn/rGO, (f) 20%CuZn/rGO and (g) 30%CuZn/rGO.





**Fig. 5.** FTIR spectra of (a) GO, (b) rGO, (c) calcined rGO, (d) 5% CuZn/rGO, (e) 10% CuZn/rGO, (f) 20%CuZn/rGO and (g) 30%CuZn/rGO.

according to the following equation:

$$L_a(\text{nm}) = \frac{560}{E_l^4} \left( \frac{I_D}{I_G} \right)^{-1} \quad (4)$$

where  $E_l$ ,  $I_D$ , and  $I_G$  are the excitation laser energy in eV ( $E_l = 2.33$  eV at  $\lambda = 532$  nm), intensities of the D and G bands, respectively. The in-plane size  $L_a$  was calculated to be 17.1 nm for rGO, 18.1 nm for rGO after calcination, and 17.7 nm for rGO after loading of bimetallic compounds of Cu-Zn [69]. This is the same order of magnitude as the crystallite size accessed from the XRD analysis of the rGO, rGO after calcination, and after loading of bimetallic compounds of Cu-Zn ( $L_a = 4.5$ , 5.4, and 4.9 nm, respectively). In conclusion, the results from the Raman spectra confirm that the structure of rGO does not change after calcination and with the presence of bimetallic compounds of Cu-Zn.

Fig. 5 shows the FTIR spectra of the catalyst samples. The presence of the peak at  $\sim 1560 \text{ cm}^{-1}$  is attributed to the skeletal vibration from the aromatic C=C stretching bands. Meanwhile, the vibration and deformation bands of O—H are found at  $\sim 3420 \text{ cm}^{-1}$ , the stretching vibration band of C=O at  $\sim 1700 \text{ cm}^{-1}$ , the stretching vibration band of C—OH at  $1200 \text{ cm}^{-1}$  and the stretching vibration band of C—O at  $1040 \text{ cm}^{-1}$ , which is in good agreement with the previous study [70]. These results confirm that the structures of both the calcined rGO and Cu-Zn loaded rGO do not change. It should be remarked that the two small peaks at  $2358$  and  $2332 \text{ cm}^{-1}$  were not generated from the analyzed samples, but they correspond to residual carbon dioxide from measurement conditions, and they should be ignored.

N<sub>2</sub> adsorption/desorption isotherms and the pore-size distributions of all samples were characterized, and the obtained results are shown in Fig. 6a and b, respectively. According to the IUPAC classification, the isotherm of all samples exhibited Type-IV behavior with a H3 hysteresis loop, indicating the presence of mesoporous structure and slit-shaped pores. The pore-size distribution shows predominant peak at 3.8 nm and another minor peak at 2.2 nm, denoting the presence of mesopores. BET surface area, pore volume and average pore diameter of the catalysts are shown in Table 1. The BET surface areas of rGO, rGO-calcined, 5% CuZn/rGO, 10% CuZn/rGO, 20% CuZn/rGO, and 30% CuZn/rGO are 57.9, 117.3, 65.6, 82.7, 41.2, and 41.8 m<sup>2</sup> g<sup>-1</sup>, respectively. It should be remarked that the BET surface area of all samples is lower than the theoretical surface area (2630 m<sup>2</sup> g<sup>-1</sup>), indicating that the rGO nanosheets consist of more than one layer as indeed found from XRD analysis. The BET surface area of rGO increases when it is calcined, due to a removal of impurities,

**Table 1**

BET surface area, pore volume, and average pore diameter of Cu-Zn/rGO catalysts.

Sample	BET Surface Area (m <sup>2</sup> g <sup>-1</sup> )	Pore Volume (cm <sup>3</sup> g <sup>-1</sup> )	Average Pore Diameter (nm)
rGO	58	0.2589	4
rGO-calcined	117	0.5955	4
5%CuZn/rGO	66	0.2094	4
10%CuZn/rGO	83	0.2273	4
20%CuZn/rGO	41	0.1468	4
30%CuZn/rGO	42	0.1424	4

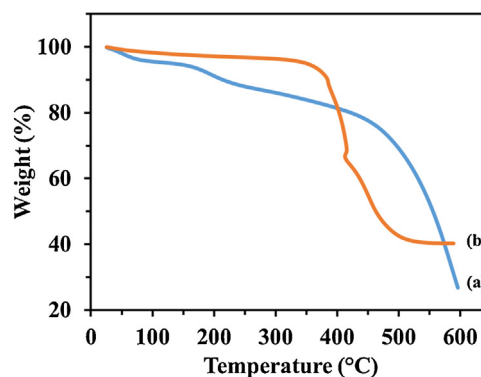


**Fig. 7.** TGA patterns of (a) rGO and (b) 30%CuZn/rGO.

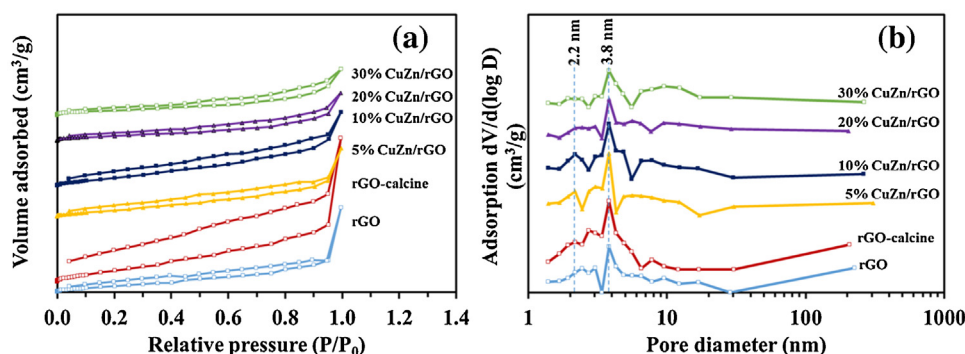


**Fig. 6.** N<sub>2</sub>-adsorption/desorption isotherms (a) and pore size distributions (b) of catalysts.

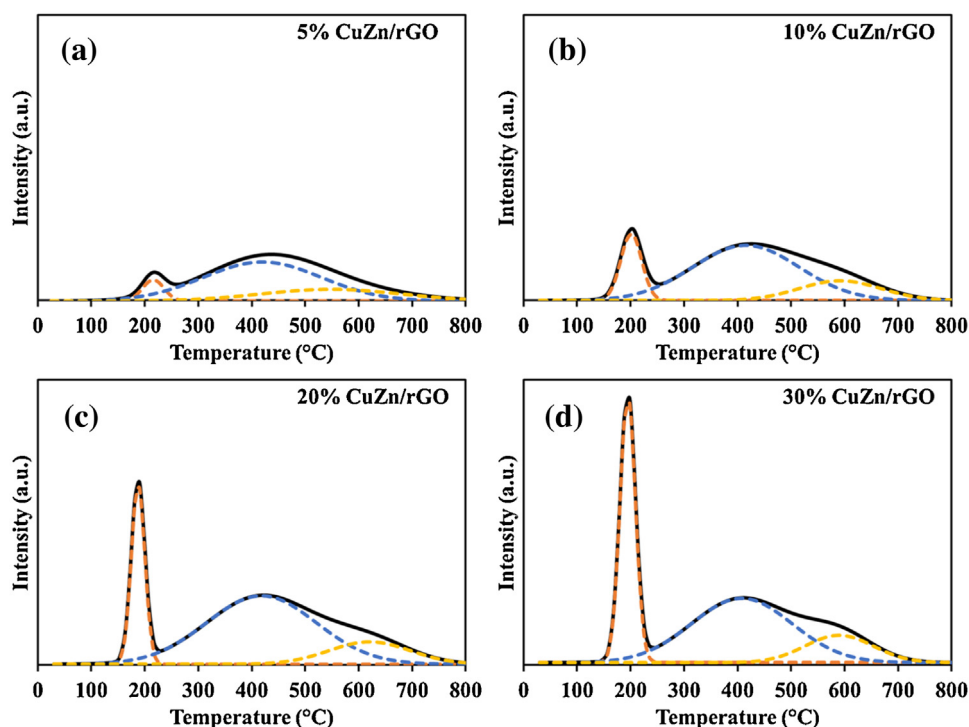


Fig. 8. H<sub>2</sub>-TPR profiles of (a) 5%CuZn/rGO, (b) 10%CuZn/rGO, (c) 20%CuZn/rGO, and (d) 30%CuZn/rGO.

leaving some pores inside the rGO and resulting in higher porosity. The samples which are loaded with bimetallic compounds of Cu-Zn contain the active metals anchored on the surfaces of rGO nanosheets. These bimetallic metals are reported to be able to prevent restacking of the rGO nanosheets [71]. One explanation of the BET surface area of 5% CuZn/rGO lower than 10% CuZn/rGO is that the amounts of the metal particles are too low to resist restacking in rGO nanosheets. By increasing the percent loading of Cu-Zn (i.e. 10 wt% Cu-Zn), the surface is slightly increased. However, at higher loadings >10 wt%, the BET surface area was found to decrease, likely caused by the agglomeration of Cu-Zn, which obscures the surface of rGO nanosheets.

The TGA patterns of the catalyst samples are shown in Fig. 7. TGA profile of rGO (Fig. 7a) implies that the first weight loss step of rGO between 100 and 200 °C could result from the desorption of physisorbed water. The next major weight loss step is observed at 450 °C and then the rGO completely decomposes at ≥600 °C. Since the major weight loss is above the calcination temperature of 350 °C, TGA can confirm that rGO was not destroyed by the calcination step. Upon addition of the bimetallic Cu-Zn compounds, TGA revealed that the percent weight loss of 30% CuZn/rGO (Fig. 7b) is lower than that of rGO because it was protected by loaded metals on its surface. The onset of weight loss occurs at 400 °C, which is lower than that of rGO, but there was no loss observed up to the calcination temperature.

The reduced behavior of the catalysts was investigated by TPR measurement, as shown in Fig. 8. The first reduction peak is related to the reduction of CuO species having the one-step reduction, Cu(II) to Cu(0), and the temperature of the peak appears in the range of 150–250 °C. The reduction peaks of the CuO species increase in intensity, which corresponds to the increase of Cu-Zn loading. In this experiment, the reduced temperature was 350 °C, bringing about the complete reduction

of CuO and partial reduction of ZnO. Consequently, the catalysts were found as Cu(0), Zn(0), and ZnO.

The surface chemical compositions of the catalysts were evaluated via XPS technique as shown in Fig. 9. The survey XPS spectrum of 10% CuZn/rGO (see Fig. 9a) shows the predominant peak of carbon (C1s) at 284.4 eV, a minor oxygen (O1s) peak at 532.4 eV, a nitrogen (N1s) peak at 400.4 eV, a copper (Cu2p) peak, and zinc (Zn2p, Zn3s, Zn3p) peak [72]. The C1s peak in the XPS spectra of 10% CuZn/rGO (Fig. 9b) can be further deconvoluted into five peaks at 284.9, 285.2, 286.4, 287.5, and 289.1 eV, which are assigned to C—C, C—N, C—O, C=O, and O—C=O groups, respectively [73,74]. This result confirms that the functional groups of GO were mostly reduced by hydrazine, and the sp<sup>3</sup> carbons in GO were converted to sp<sup>2</sup> carbons. Additionally, with the addition of bimetal, Cu-Zn, the structure of rGO (C—C) remains unchanged. From Fig. 9c, it is also observed that the Zn2p has two fitting peaks found at about 1022 and 1045 eV, corresponding to Zn2p<sub>3/2</sub>, and Zn2p<sub>1/2</sub>, respectively [75]. The spin energy separation between the Zn2p<sub>3/2</sub> and the Zn2p<sub>1/2</sub> is 23 eV. It can be indicated that the Zn atoms are in a completely oxidized state [76]. The two fitting peaks observed in the O1s region with binding energies of 531.4 and 532.8 eV are attributed to the oxidized metal ions in the nanoparticles (Fig. 9d) [77]. Fig. 9e exhibits the Cu2p XPS spectrum. The peaks appear at 934 eV and 962.9 eV, together with two peaks overlapping at 942 and 944.3 eV, which are assigned to the peak of Cu2p<sub>3/2</sub>. On the other hand, the peak occurs at 954.2 eV, corresponding to the peak of Cu2p<sub>1/2</sub>. These are attributed to the fully oxidized CuO surface [78]. The N1s spectra consist of three group peaks (Fig. 9f), which are assigned to the stretches of pyridinic-N, pyrrolic-N, graphitic-N, at binding energies of 399.2, 400.4, and 401.8 eV, respectively [79]. These nitrogen atoms can provide the lone pair electrons that can create polarity. Subsequently, the created polarity enhanced the insertion

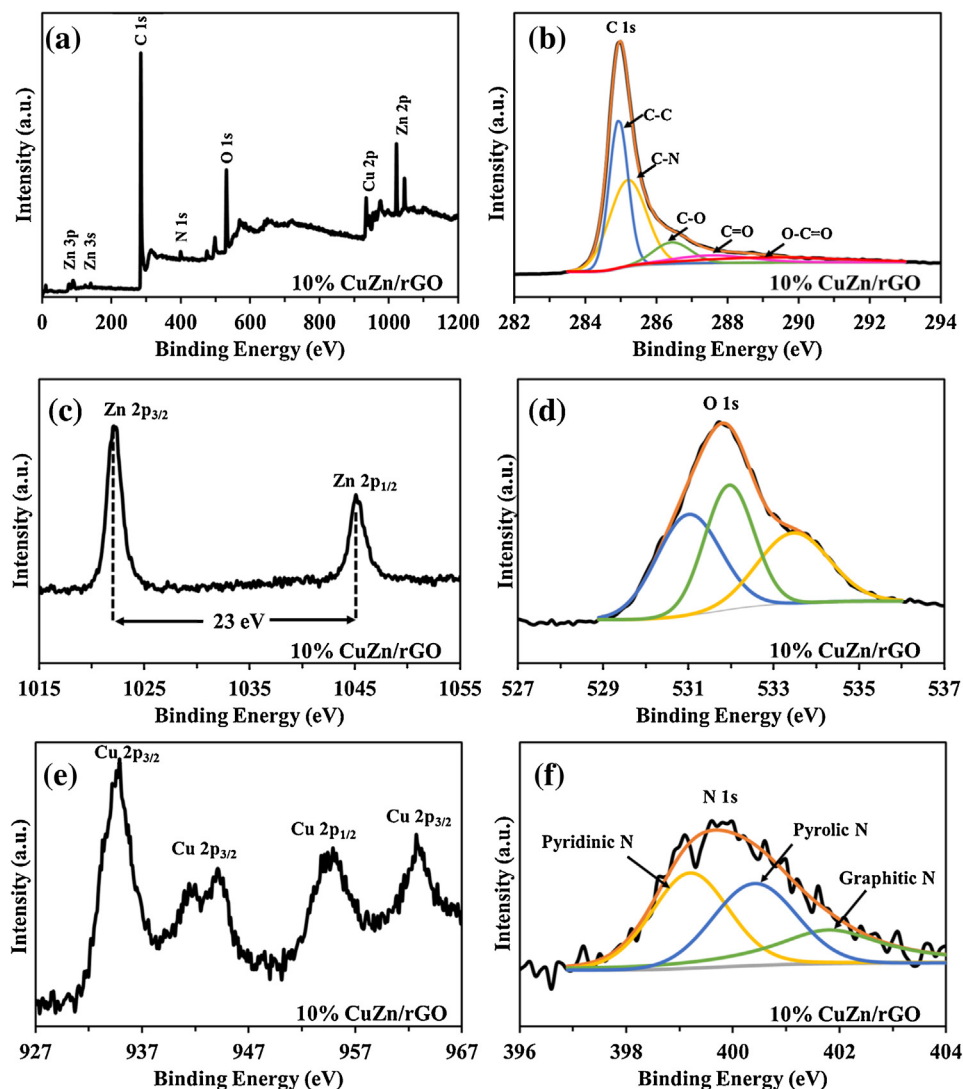


Fig. 9. XPS spectra for (a) survey spectra, (b) C 1s, (c) Zn 2p, (d) O 1s, (e) Cu 2p, and (f) N 1s of 10% CuZn/rGO.

of the copper and zinc ions in the rGO nanosheets [80,81] and formed metal complex [82].

### 3.2. Catalytic activity results

#### 3.2.1. Effect of reaction temperature

The effect of hydrogenation temperature over 30%CuZn/rGO was investigated. From Fig. 10, it shows that the space-time yield of methanol ( $STY_{MeOH}$ ) increases at reaction temperatures up to 250 °C, and then decreases above 250 °C. It can be explained that although a higher reaction temperature is preferred for CO<sub>2</sub> hydrogenation, it is possible that active metal particles agglomerated to form a larger cluster at a temperature above 250 °C. Consequently, the reaction temperature of 250 °C, which gave the highest space-time yield of methanol, was chosen for the activity testing of other catalysts.

#### 3.2.2. Catalytic performance

The catalytic performance of the catalysts for CO<sub>2</sub> hydrogenation to methanol is summarized in Table 2. The 10 wt%CuZn/rGO catalyst exhibits the highest activity for the hydrogenation of CO<sub>2</sub> with a 26% CO<sub>2</sub> conversion, 5.1% MeOH selectivity, and  $424 \pm 18$

$mg_{MeOH} g_{cat}^{-1} h^{-1} STY_{MeOH}$  at 250 °C and 15 bar after 5 h on stream of CO<sub>2</sub> and H<sub>2</sub>. When the reaction was over, the spent catalyst was re-examined its structure with an XRD, in order to assess the stability of rGO. The obtained XRD pattern (not shown here) reveals that the catalyst still has the same structure as that of the

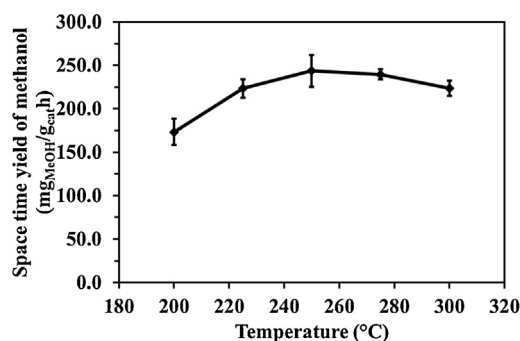


Fig. 10. Space time yield of methanol as a function of temperature, using 30%Cu-Zn/rGO catalyst.

**Table 2**The catalytic performance of CO<sub>2</sub> hydrogenation to methanol at 250 °C and 15 bar (average over 5 h).

Sample	CO <sub>2</sub> conversion (%)	CH <sub>3</sub> OH selectivity (%)	CO selectivity (%)	CH <sub>4</sub> selectivity (%)	STY of CH <sub>3</sub> OH (mg/g <sub>cat</sub> h))
5%CuZn/rGO	14	2.8	69.2	11.1	220
10%CuZn/rGO	26	5.1	33.9	7.1	424
20%CuZn/rGO	19	8.5	55.9	15.0	244
30%CuZn/rGO	20	15.6	62.4	16.0	244

**Table 3**Comparison of the obtained performance on CO<sub>2</sub> hydrogenation to methanol with previous published works.

Catalysts	CO <sub>2</sub> Conv. (%)	STY <sub>CH<sub>3</sub>OH</sub> (mg/g <sub>cat</sub> h)	Condition T (°C)/P (bar)	Reference
CuZnGa	15.8	135	270/30	[17]
Cu-ZnO/Al <sub>2</sub> O <sub>3</sub>	9.4	11	250/20	[31]
Cu-Zn/SiO <sub>2</sub>	2.0	66	250/20	[37]
16%Pd <sub>0.1</sub> Zn <sub>1</sub> /CNTs	6.2	37	220/80	[50]
Cu-ZnO	11.2	9	250/30	[83]
Cu/ZnO/ZrO <sub>2</sub>	24.6	210	270/50	[84]
10Cu60Zn30	21.0	274	250/15	[85]
10%CuZn/rGO	26.0	424	250/15	This work

fresh catalyst. When increasing the loading beyond 10 wt%, the CO<sub>2</sub> conversion and STY<sub>MeOH</sub> decreased because the agglomeration of active metals led to reduced copper oxides to metallic Cu<sup>0</sup>, which is a crucial active metal for methanol synthesis.

Regarding the other works, the achieved performance by this work was compared to those of previous published works [17,31,37,50,83–85] as shown in Table 3. It is clearly seen that this work gives the highest STY<sub>MeOH</sub> under the lowest operating pressure. As the matter of fact, the rGO, reduced by hydrazine, plays very important role in the enhanced performance of the CuZn/rGO catalyst. Refer to the XPS analysis as described earlier, the nitrogen atoms that linked with the rGO can reduce the energy barrier of H<sub>2</sub> dissociation [86,87]. It was reported that pyridinic-N is a favorable site for hydrogen bond interaction, which can attract hydrogen donor molecule to increase the STY<sub>MeOH</sub> [88]. In addition, nitrogen groups can transfer multiple electrons, which involve in the conversion of CO<sub>2</sub> to methanol [89,90]. As a comparison, only a bulk Cu-ZnO catalyst gives a STY<sub>MeOH</sub> less than 9 mg<sub>MeOH</sub> g<sub>cat</sub><sup>−1</sup> h<sup>−1</sup> [83,91].

#### 4. Conclusions

rGO nanosheets with diluted oxygen-containing groups were for the first time used as the support of the bimetallic Cu-Zn catalysts. The catalytic performances of the as-synthesized catalysts on the rGO support were investigated toward the CO<sub>2</sub> hydrogenation reaction to methanol fuel. The effects of the quantity of Cu-Zn loaded onto rGO support and the reaction temperature for converting CO<sub>2</sub> to methanol were studied using a tubular stainless steel fixed-bed reactor. The gas products were subsequently investigated by the gas chromatography technique. The investigation showed that increasing the reaction temperature over 250 °C can obstruct the methanol synthesis by decreasing the space time yield of methanol. Increasing the loading content of bimetallic compounds Cu and Zn over 10 wt% can lead to the undesired aggregation, less dispersion, and low specific surface area, eventually exhibiting poor catalytic activity with low space-time yield of methanol. After finely tuned, the rGO-supported Cu-Zn catalyst can provide the highest catalytic performance toward the CO<sub>2</sub> hydrogenation to methanol at a reaction temperature of 250 °C and a loading content of 10 wt% Cu and Zn metals on the rGO support. The catalyst provides the highest methanol productivity

of 424 mg<sub>MeOH</sub> g<sub>cat</sub><sup>−1</sup> h<sup>−1</sup>, which may lead to the practical CO<sub>2</sub> conversion to methanol.

#### Acknowledgements

This research was supported by the Faculty of Engineering, Kasetsart University (scholarship for Varisara Deetratrakul) and the Kasetsart University Research and Development Institute (KURDI).

#### References

- [1] E.H. Bennetzen, P. Smith, J.R. Porter, Agricultural production and greenhouse gas emissions from world regions—the major trends over 40 years, *Global Environ. Change* 37 (2016) 43–55.
- [2] S. Gai, J. Yu, H. Yu, J. Eagle, H. Zhao, J. Lucas, E. Doroodchi, B. Moghtaderi, Process simulation of a near-zero-carbon-emission power plant using CO<sub>2</sub> as the renewable energy storage medium, *Int. J. Greenh. Gas Control* 47 (2016) 240–249.
- [3] O. Akbilgic, G. Doluweera, M. Mahmoudkhani, J. Bergerson, A meta-analysis of carbon capture and storage technology assessments: understanding the driving factors of variability in cost estimates, *Appl. Energy* 159 (2015) 11–18.
- [4] P. Markewitz, W. Kuckshinrichs, W. Leitner, J. Linssen, P. Zapp, R. Bongartz, A. Schreiber, T.E. Muller, Worldwide innovations in the development of carbon capture technologies and the utilization of CO<sub>2</sub>, *Energy Environ. Sci.* 5 (2012) 7281–7305.
- [5] M. Pérez-Fortes, J.C. Schöneberger, A. Boulamanti, E. Tzimas, Methanol synthesis using captured CO<sub>2</sub> as raw material: techno-economic and environmental assessment, *Appl. Energy* 161 (2016) 718–732.
- [6] M.M.F. Hasan, E.L. First, F. Boukouvala, C.A. Floudas, A multi-scale framework for CO<sub>2</sub> capture, utilization, and sequestration: CCUS and CCU, *Comput. Chem. Eng.* 81 (2015) 2–21.
- [7] M.T. Luu, D. Milani, A. Abbas, Analysis of CO<sub>2</sub> utilization for methanol synthesis integrated with enhanced gas recovery, *J. Clean. Prod.* 112 (2016) 3540–3554.
- [8] J. Toyir, P. Ramirez de la Piscina, N. Homs, Ga-promoted copper-based catalysts highly selective for methanol steam reforming to hydrogen; relation with the hydrogenation of CO<sub>2</sub> to methanol, *Int. J. Hydrogen Energy* 40 (2015) 11261–11266.
- [9] E.L. Kunkes, F. Studt, F. Abild-Pedersen, R. Schlögl, M. Behrens, Hydrogenation of CO<sub>2</sub> to methanol and CO on Cu/ZnO/Al<sub>2</sub>O<sub>3</sub>: Is there a common intermediate or not? *J. Catal.* 328 (2015) 43–48.
- [10] G.A. Olah, Towards oil independence through renewable methanol chemistry, *Angew. Chem. Int. Ed.* 52 (2013) 104–107.
- [11] L. Li, D. Mao, J. Yu, X. Guo, E. Miró, Highly selective hydrogenation of CO<sub>2</sub> to methanol over CuO–ZnO–ZrO<sub>2</sub> catalysts prepared by a surfactant-assisted coprecipitation method, *J. Power Sources* 279 (2015) 394–404.
- [12] X. Jiang, N. Koizumi, X. Guo, C. Song, Bimetallic Pd–Cu catalysts for selective CO<sub>2</sub> hydrogenation to methanol, *Appl. Catal., B* 170–171 (2015) 173–185.
- [13] S. Pimprom, K. Sriboonkham, P. Dittanet, K. Föttinger, G. Rupprechter, P. Kongkachuichay, Synthesis of copper-nickel/SBA-15 from rice husk ash catalyst for dimethyl carbonate production from methanol and carbon dioxide, *J. Ind. Eng. Chem.* 31 (2015) 156–166.
- [14] W. Wang, S. Wang, X. Ma, J. Gong, Recent advances in catalytic hydrogenation of carbon dioxide, *Chem. Soc. Rev.* 40 (2011) 3703–3727.
- [15] X. Guo, D. Mao, S. Wang, G. Wu, G. Lu, Combustion synthesis of CuO–ZnO–ZrO<sub>2</sub> catalysts for the hydrogenation of carbon dioxide to methanol, *Catal. Commun.* 10 (2009) 1661–1664.
- [16] A.A. Kiss, J.J. Prag, H.J. Vos, G. Bargeman, M.T. de Groot, Novel efficient process for methanol synthesis by CO<sub>2</sub> hydrogenation, *Chem. Eng. J.* 284 (2016) 260–269.
- [17] W. Cai, P.R. de la Piscina, J. Toyir, N. Homs, CO<sub>2</sub> hydrogenation to methanol over CuZnGa catalysts prepared using microwave-assisted methods, *Catal. Today* 242 (2015) 193–199.
- [18] Y. Hartadi, D. Widmann, R.J. Behm, Methanol formation by CO<sub>2</sub> hydrogenation on Au/ZnO catalysts—effect of total pressure and influence of CO on the reaction characteristics, *J. Catal.* 333 (2016) 238–250.
- [19] S. Saeidi, N.A.S. Amin, M.R. Rahimpour, Hydrogenation of CO<sub>2</sub> to value-added products—a review and potential future developments, *J. CO<sub>2</sub> Util.* 5 (2014) 66–81.



- [20] M. Aresta, A. Dibenedetto, E. Quaranta, *Reaction Mechanisms in Carbon Dioxide Conversion*, Springer, New York, 2016.
- [21] N.A.M. Razali, K.T. Lee, S. Bhatia, A.R. Mohamed, Heterogeneous catalysts for production of chemicals using carbon dioxide as raw material: a review, *Renew. Sustain. Energy Rev.* 16 (2012) 4951–4964.
- [22] A.S. Aquino, F.L. Bernard, M.O. Vieira, J.V. Borges, M.F. Rojas, F.D. Vecchia, R.A. Ligabue, M. Seferin, S. Menezes, S. Einloft, A new approach to CO<sub>2</sub> capture and conversion using imidazolium based-ionic liquids as sorbent and catalyst, *J. Braz. Chem. Soc.* 25 (2014) 2251–2257.
- [23] G. Centi, S. Perathoner, Carbon dioxide utilization for global sustainability, *Stud. Surf. Sci. Catal.* 153 (2004) 1–8.
- [24] C. Song, Global challenges and strategies for control conversion and utilization of CO<sub>2</sub> for sustainable development involving energy, catalysis, adsorption and chemical processing, *Catal. Today* 115 (2006) 2–32.
- [25] H. Lei, R. Nie, G. Wu, Z. Hou, Hydrogenation of CO<sub>2</sub> to CH<sub>3</sub>OH over Cu/ZnO catalysts with different ZnO morphology, *Fuel* 154 (2015) 161–166.
- [26] J. Yoshihara, C.T. Campbell, Methanol synthesis and reverse water–gas shift kinetics over Cu(110) model catalysts: Structural sensitivity, *J. Catal.* 161 (1996) 776–782.
- [27] A.M. Beale, E.K. Gibson, M.G. O'Brien, S.D.M. Jacques, R.J. Cernik, M.D. Michiel, P.D. Cobden, Ö. Pirgon-Galin, L.V.D. Water, M.J. Watson, B.M. Weckhuysen, Chemical imaging of the sulfur-induced deactivation of Cu/ZnO catalyst bodies, *J. Catal.* 314 (2014) 94–100.
- [28] M. Behrens, F. Studt, I. Kasatkin, S. Kühl, M. Hävecker, F. Abild-Pedersen, S. Zander, F. Girgsdies, P. Kurr, B.L. Kniep, M. Tovar, R.W. Fischer, J.K. Nørskov, R. Schlögl, The active site of methanol synthesis over Cu/ZnO/Al<sub>2</sub>O<sub>3</sub> industrial catalysts, *Science* 336 (2012) 893–897.
- [29] H.Y. Chen, S.P. Lau, L. Chen, J. Lin, C.H.A. Huan, K.L. Tan, J.S. Pan, Synergism between Cu and Zn sites in Cu/Zn catalysts for methanol synthesis, *Appl. Surf. Sci.* 152 (1999) 193–199.
- [30] M.S. Spencer, The role of zinc oxide in Cu/ZnO catalysts for methanol synthesis and the water–gas shift reaction, *Top. Catal.* 8 (1999) 259–266.
- [31] H. Ren, C.H. Xu, H.Y. Zhao, Y.X. Wang, J. Liu, J.Y. Liu, Methanol synthesis from CO<sub>2</sub> hydrogenation over Cu/γ-Al<sub>2</sub>O<sub>3</sub> catalysts modified by ZnO, ZrO<sub>2</sub> and MgO, *J. Ind. Eng. Chem.* 28 (2015) 261–267.
- [32] Y. Okamoto, K. Fukino, T. Imanaka, S. Teranishi, Synergy between Cu and ZnO for methanol conversions over Cu–ZnO catalysts, *Chem. Lett.* 13 (1984) 71–74.
- [33] J. Nakamura, T. Uchijima, Y. Kanai, T. Fujitani, The role of ZnO in Cu/ZnO methanol synthesis catalysts, *Catal. Today* 28 (1996) 223–230.
- [34] F. Arena, G. Italiano, K. Barbera, S. Bordiga, G. Bonura, L. Spadaro, F. Frusteri, Solid-state interactions, adsorption sites and functionality of Cu–ZnO/ZrO<sub>2</sub> catalysts in the CO<sub>2</sub> hydrogenation to CH<sub>3</sub>OH, *Appl. Catal. A* 350 (2008) 16–23.
- [35] J. Agrell, M. Boutonnet, I. Melián-Cabrera, J.L.G. Fierro, Production of hydrogen from methanol over binary Cu/ZnO catalysts part I. Catalyst preparation and characterization, *Appl. Catal. A* 253 (2003) 201–211.
- [36] G. Bonura, M. Cordaro, C. Cannilla, F. Arena, F. Frusteri, The changing nature of the active site of Cu–Zn–Zr catalysts for the CO<sub>2</sub> hydrogenation reaction to methanol, *Appl. Catal. B: Environ.* 152–153 (2014) 152–161.
- [37] J. Toyir, P.R. de la Piscina, J.L.G. Fierro, N.S. Homs, Highly effective conversion of CO<sub>2</sub> to methanol over supported and promoted copper-based catalysts: influence of support and promoter, *Appl. Catal. B* 29 (2001) 207–215.
- [38] X.M. Liu, G.Q. Lu, Z.F. Yan, J. Beltrami, Recent advances in catalysts for methanol synthesis via hydrogenation of CO and CO<sub>2</sub>, *Ind. Eng. Chem. Res.* 42 (2003) 6518–6530.
- [39] V.R. Surisetty, A.K. Dalai, J. Kozinski, Influence of porous characteristics of the carbon support on alkali-modified trimetallic Co–Rh–Mo sulfided catalysts for higher alcohols synthesis from synthesis gas, *Appl. Catal. A* 393 (2011) 50–58.
- [40] J. Xiao, D. Mao, X. Guo, J. Yu, Effect of TiO<sub>2</sub>, ZrO<sub>2</sub>, and TiO<sub>2</sub>/ZrO<sub>2</sub> on the performance of CuO–ZnO catalyst for CO<sub>2</sub> hydrogenation to methanol, *Appl. Surf. Sci.* 338 (2015) 146–153.
- [41] R. Burch, R.J. Chappell, S.E. Golunski, Synergy at a distance in the synthesis of methanol over copper catalysts, *Catal. Lett.* 1 (1988) 439–443.
- [42] R. Burch, S.E. Golunski, M.S. Spencer, The role of hydrogen in methanol synthesis over copper catalysts, *Catal. Lett.* 5 (1990) 55–60.
- [43] L. Angelo, K. Kobi, L.M.M. Tejada, Y. Zimmermann, K. Parkhomenko, A.C. Roger, Study of CuZnMo<sub>x</sub> oxides (M = Al, Zr Ce, CeZr) for the catalytic hydrogenation of CO<sub>2</sub> into methanol, *C. R. Chim.* 18 (2015) 250–260.
- [44] T.O. Eschemann, W.S. Lamme, R.L. Manchester, T.E. Parmentier, A. Cognigni, M. Rønning, K.P. de Jong, Effect of support surface treatment on the synthesis, structure, and performance of Co/CNT Fischer-Tropsch catalysts, *J. Catal.* 328 (2015) 130–138.
- [45] E.Y.L. Theo, L. Muniandy, E.P. Ng, F. Adam, A.R. Mohamed, R. Jose, K.F. Chong, High surface area activated carbon from rice husk as a high performance supercapacitor electrode, *Electrochim. Acta* 192 (2016) 110–119.
- [46] D. Kalpana, S.H. Cho, S.B. Lee, Y.S. Lee, R. Misra, N.G. Renganathan, Recycled waste paper—a new source of raw material for electric double-layer capacitors, *J. Power Sources* 190 (2009) 587–591.
- [47] G. Wang, L. Chen, Y. Sun, J. Wu, M. Fu, D. Ye, Carbon dioxide hydrogenation to methanol over Cu/ZrO<sub>2</sub>/CNTs: effect of carbon surface chemistry, *RSC Adv.* 5 (2015) 45320–45330.
- [48] F. Rodríguez-Reinos, The role of carbon materials in heterogeneous catalysis, *Carbon* 36 (1998) 159–175.
- [49] S. Liu, S. Zhao, Y. Yao, P. Dong, C. Yang, Crystallized hybrid carbon synthesized by catalytic carbonization of biomass and in-situ growth of carbon nanofibers, *J. Mater. Sci. Technol.* 30 (2014) 466–472.
- [50] X.L. Liang, X. Dong, G.D. Lin, H.B. Zhang, Carbon nanotube-supported Pd–ZnO catalyst for hydrogenation of CO<sub>2</sub> to methanol, *Appl. Catal. B* 88 (2009) 315–322.
- [51] G. Wu, X. Wang, N. Guan, L. Li, Palladium on graphene as efficient catalyst for solvent-free aerobic oxidation of aromatic alcohols: role of graphene support, *Appl. Catal. B* 136–137 (2013) 177–185.
- [52] K.S. Novoselov, A.K. Geim, S.V. Morozov, D. Jiang, Y. Zhang, S.V. Dubonos, A.A. Firsov, Electric field effect in atomically thin carbon films, *Science* 306 (2004) 666–669.
- [53] T. Kuila, S. Bose, A.K. Mishra, P. Khanra, N.H. Kim, J.H. Lee, Chemical functionalization of graphene and its applications, *Prog. Mater. Sci.* 57 (2012) 1061–1105.
- [54] L. Wen, Z. Song, J. Ma, W. Meng, X. Qin, Low-temperature synthesis of few-layer graphene, *Mater. Lett.* 160 (2015) 255–258.
- [55] Z.H. Ni, L.A. Ponomarenko, R.R. Nair, R. Yang, S. Anissimova, I.V. Grigorieva, F. Schedin, P. Blake, Z.X. Shen, E.H. Hill, K.S. Novoselov, A.K. Geim, On resonant scatters as a factor limiting carrier mobility in graphene, *Nano Lett.* 10 (2010) 3868–3872.
- [56] D.H. Lee, J.E. Kim, T.H. Han, J.W. Hwang, S. Jeon, S.Y. Choi, S.H. Hong, W.J. Lee, R. S. Ruoff, S.O. Kim, Versatile carbon hybrid films composed of vertical carbon nanotubes grown on mechanically compliant graphene films, *Adv. Mater.* 22 (2010) 1247–1252.
- [57] A.A. Balandin, S. Ghosh, W. Bao, I. Calizo, D. Teweldebrhan, F. Miao, C.N. Lau, Superior thermal conductivity of single-layer graphene, *Nano Lett.* 8 (2008) 902–907.
- [58] W.S. Hummer, R.E. Offeman, Preparation of graphitic oxide, *J. Am. Chem. Soc.* 80 (1958) 1339.
- [59] M. Sawangphruk, P. Srimuk, P. Chiochan, A. Kittayavathananon, S. Luanwuthi, J. Limtrakul, High-performance supercapacitor of manganese oxide/reduced graphene oxide nanocomposite coated on flexible carbon fiber paper, *Carbon* 60 (2013) 109–116.
- [60] Y. Ren, J. Wang, X. Huang, J. Ding, The synthesis of polypyrrole@Mn<sub>3</sub>O<sub>4</sub>/reduced graphene oxide anode with improved coulombic efficiency, *Electrochim. Acta* 186 (2015) 345–352.
- [61] K. Krishnamoorthy, M. Veerapandian, K. Yun, S.J. Kim, The chemical and structural analysis of graphene oxide with different degrees of oxidation, *Carbon* 53 (2013) 38–49.
- [62] T. Ungár, J. Gubicza, G. Ribárik, C. Pantea, T.W. Zerda, Microstructure of carbon blacks determined by X-ray diffraction profile analysis, *Carbon* 40 (2002) 929–937.
- [63] Z.Q. Li, C.J. Lu, Z.P. Xia, Y. Zhou, Z. Luo, X-ray diffraction patterns of graphite and turbostratic carbon, *Carbon* 45 (2007) 1686–1695.
- [64] M.B. Lim, M. Hu, S. Manandhar, A. Sakshaug, A. Strong, L. Riley, P.J. Pauzauskie, Ultrafast sole–gel synthesis of graphene aerogel materials, *Carbon* 95 (2015) 616–624.
- [65] S. Stankovich, D.A. Dikin, R.D. Piner, K.A. Kohlhaas, A. Kleinhammes, Y. Jia, Y. Wu, S.T. Nguyen, R.S. Ruoff, Synthesis of graphene-based nanosheets via chemical reduction of exfoliated graphite oxide, *Carbon* 45 (2007) 1558–1565.
- [66] M.C. Hsiao, S.H. Liao, M.Y. Yen, P.I. Liu, N.W. Pu, C.A. Wang, C.C.M. Ma, Preparation of covalently functionalized graphene using residual oxygen-containing functional groups, *ACS Appl. Mater. Interfaces* 2 (2010) 3092–3099.
- [67] M. Sawangphruk, P. Srimuk, P. Chiochan, T. Sangsri, P. Siwayaprahm, Synthesis and antifungal activity of reduced graphene oxide nanosheets, *Carbon* 50 (2012) 5156–5161.
- [68] J.M. Mativetsky, E. Treossi, E. Orgiu, M. Melucci, G.P. Veronese, P. Samorì, V. Palermo, Local current mapping and patterning of reduced graphene oxide, *J. Am. Chem. Soc.* 132 (2010) 14130–14136.
- [69] L.G. Cançado, K. Takai, T. Enoki, M. Endo, Y.A. Kim, H. Mizusaki, A. Jorio, L.N. Coelho, R. Magalhães-Paniago, M.A. Pimenta, General equation for the determination of the crystallite size L<sub>a</sub> of nanographite by Raman spectroscopy, *Appl. Phys. Lett.* 88 (2006) 163106.
- [70] X. Zhou, J. Zhang, H. Wu, H. Yang, J. Zhang, S. Guo, Reducing graphene oxide via hydroxylamine: a simple and efficient route to graphene, *J. Phys. Chem. C* 115 (2011) 11957–11961.
- [71] Y. Wang, Y. Wu, Y. Huang, F. Zhang, X. Yang, Y. Ma, Y. Chen, Preventing graphene sheets from restacking for high-capacitance performance, *J. Phys. Chem. C* 115 (2011) 23192–23197.
- [72] H. Fang, L. Zhao, W. Yue, Y. Wang, Y. Jiang, Y. Zhang, Facile and large-scale preparation of sandwich-structured graphene-metal oxide composites as anode materials for Li-ion batteries, *Electrochim. Acta* 186 (2015) 397–403.
- [73] K. Wang, X. Dong, C. Zhao, X. Qian, Y. Xu, Facile synthesis of Cu<sub>2</sub>O/CuO/RGO nanocomposite and its superior cyclability in supercapacitor, *Electrochim. Acta* 152 (2015) 433–442.
- [74] N.B. Trung, T.V. Tam, H.R. Kim, S.H. Hur, E.J. Kim, W.M. Choi, Three-dimensional hollow balls of graphene-polyaniline hybrids for supercapacitor applications, *Chem. Eng. J.* 255 (2014) 89–96.
- [75] O. Lupan, G.A. Emelchenko, V.V. Ursaki, G. Chai, A.N. Redkin, A.N. Gruzintsev, I. M. Tiginyanu, L. Chow, L.K. Ono, B. Roldan Cuenya, H. Heinrich, E.E. Yakimov, Synthesis and characterization of ZnO nanowires for nanosensor applications, *Mater. Res. Bull.* 45 (2010) 1026–1032.
- [76] R. Al-Gaashani, S. Radiman, A.R. Daud, N. Tabet, Y. Al-Douri, XPS and optical studies of different morphologies of ZnO nanostructures prepared by microwave methods, *Ceram. Int.* 39 (2013) 2283–2292.
- [77] A. Saaedi, R. Yousefi, F. Jamali-Sheini, A.K. Zak, M. Cheraghizade, M.R. Mahmoodian, M.A. Baghchesara, A.S. Dezaki, XPS studies and photocurrent

- applications of alkali metals-doped ZnO nanoparticles under visible illumination conditions, *Physica E* 79 (2016) 113–118.
- [78] S. Poulston, P.M. Parlett, P. Stone, M. Bowker, Surface oxidation and reduction of CuO and Cu<sub>2</sub>O studied using XPS and XAES, *Surf. Interface Anal.* 24 (1996) 811–820.
- [79] P. Iamprasertkun, A. Krittayavathananon, M. Sawangphruk, N-doped reduced graphene oxide aerogel coated on carboxyl-modified carbon fiber paper for high-performance ionic liquid supercapacitors, *Carbon* 102 (2016) 455–461.
- [80] H. Xu, J. Xiao, B. Liu, S. Griveau, F. Bedioui, Enhanced electrochemical sensing of thiols based on cobalt phthalocyanine immobilized on nitrogen-doped graphene, *Biosens. Bioelectron.* 66 (2015) 438–444.
- [81] P. Kumar, H.P. Mungse, O.P. Khatri, S.L. Jain, Nitrogen-doped graphene-supported copper complex: a novel photocatalyst for CO<sub>2</sub> reduction under visible light irradiation, *RSC Adv.* 5 (2015) 54929–54935.
- [82] S.Q. Liu, S.S. Zhou, Z.G. Chen, C.B. Liu, F. Chen, Z.Y. Wu, An artificial photosynthesis system based on CeO<sub>2</sub> as light harvester and N-doped graphene Cu(II) complex as artificial metalloenzyme for CO<sub>2</sub> reduction to methanol fuel, *Catal. Commun.* 73 (2016) 7–11.
- [83] H. Jeong, C. Cho, T. Kim, Effect of Zr and pH in the preparation of Cu/ZnO catalysts for the methanol synthesis by CO<sub>2</sub> hydrogenation, *Reac. Kinet. Mech. Cat.* 106 (2012) 435–443.
- [84] X. Dong, F. Li, N. Zhao, F. Xiao, J. Wang, Y. Tan, CO<sub>2</sub> hydrogenation to methanol over Cu/ZnO/ZrO<sub>2</sub> catalysts prepared by precipitation-reduction method, *Appl. Catal. B* 191 (2016) 8–17.
- [85] J. Siwawut, P. Namkhang, P. Kongkachuichay, Co-metal catalysts (Cu, Zn, Al) on SiO<sub>2</sub>-TiO<sub>2</sub> for methanol production from CO<sub>2</sub>: effect of preparation methods, *Chem. Eng. Technol.* 38 (2015) 2153–2160.
- [86] T. Liao, C. Sun, Z. Sun, A. Du, S. Smith, Chemically modified ribbon edge stimulated H<sub>2</sub> dissociation: a first-principles computational study, *Phys. Chem. Chem. Phys.* 15 (2013) 8054–8057.
- [87] J. Albero, H. Garcia, Doped graphenes in catalysis, *J. Mol. Catal. A: Chem.* 408 (2015) 296–309.
- [88] L.K. Putri, W.J. Ong, W.S. Chang, S.P. Chai, Heteroatom doped graphene in photocatalysis: a review, *Appl. Surf. Sci.* 358 (2015) 2–14.
- [89] L.P. Zhang, Z.H. Xia, Mechanisms of oxygen reduction reaction on nitrogen-doped graphene for fuel cells, *J. Phys. Chem. C* 115 (2011) 11170–11176.
- [90] L. Yu, X. Pan, X. Cao, P. Hu, X.J. Bao, Oxygen reduction reaction mechanism on nitrogen-doped graphene: a density functional theory study, *J. Catal.* 282 (2011) 183–190.
- [91] A. Karelavic, A. Bargibant, C. Fernández, P. Ruiz, Effect of the structural and morphological properties of Cu/ZnO catalysts prepared by citrate method on their activity toward methanol synthesis from CO<sub>2</sub> and H<sub>2</sub> under mild reaction conditions, *Catal. Today* 197 (2012) 109–118.